Materials Characterization 148 (2019) 178–187

Contents lists available at ScienceDirect

Materials Characterization

journal homepage: www.elsevier.com/locate/matchar

Characterization of nanoscale precipitates in superalloy 718 using high resolution SEM imaging

T.M. Smith[a,*], N.M. Senanayake[b], C.K. Sudbrack[c], P. Bonacuse[a], R.B. Rogers[a], P. Chao[d], J. Carter[b]

[a] NASA Glenn Research Center, Materials and Structures Division, Cleveland, OH 44135, United States of America
[b] Case Western Reserve University, Department of Materials Science and Engineering, Cleveland, OH 44106, United States of America
[c] QuesTek Innovations LLC, Evanston, IL 60201, United States of America
[d] Carnegie Mellon University, Department of Materials Science and Engineering, Pittsburgh, PA 15213, United States of America

ARTICLE INFO

Keywords:
Superalloy 718
Precipitate characterization
SEM
STEM-EDS
Automated image processing

ABSTRACT

At present, obtaining accurate volume fraction and size measurements of γ″, γ′, and δ precipitates in Superalloy 718 has been challenging due to their size, crystal structures, low volume fractions, and similar chemistries. These measurements are necessary to validate precipitation models that in turn enhance selective laser melting fabrication. Superalloy 718 is a promising candidate for selective laser melting fabrication due to a combination of excellent mechanical properties and workability. A new technique, combining high resolution distortion corrected SEM imaging and with high resolution x-ray energy dispersive spectroscopy, has been developed to accurately and independently measure the size, volume fraction, and number densities of these three precipitates. A specimen of selective laser melted superalloy 718 was obtained and underwent a conventional heat treatment for superalloy 718 where it was solutionized at 1010 °C for one hour, gas quenched and followed by a two-step age (718 °C/11 h → 621 °C/6 h) in order to produce a microstructure with all three precipitate types present. These results were further validated using x-ray diffraction and phase extraction methods.

1. Introduction

Superalloy 718, which consists of the base composition (51Ni-22Fe-19Cr-5Nb-3Mo-1Co-1Ti-.5Al), is a promising candidate for additive manufacturing (AM) for both its high temperature and welding properties [1–3]. Three intermetallic phases γ″ (Ni_3Nb - DO_{22} crystal structure), γ′ (Ni_3Al,Nb - $L1_2$ crystal structure), and δ (Ni_3Nb - DO_a crystal structure) all contribute overall favorable high temperature properties of the superalloy; though it is primarily considered a γ″ strengthened superalloy [4–7]. Like many superalloys, post-processing heat treatments are applied to superalloy 718 to obtain optimal mechanical properties in accordance with established standards, e.g. [8]. In an effort to reduce cost and shorten production schedule, NASA is pursuing selective laser melting (SLM) 718 components for its Space Launch System engines, and is developing a number of modeling tools to understand SLM 718 fabrication, process control and microstructure, including predicting SLM 718 microstructures with CALPHAD-based software after varying post-processing steps. Accurately tuning and validating CALPHAD-based modeling requires precise microstructural measurements of the precipitate dimensions, volume fractions and number densities. However, due to the nanoscale size, morphology, and chemical similarities of the γ″, γ′, and δ phases, this characterization becomes a problematic exercise [9–11]. Because of these issues, many superalloy 718 characterization studies do not quantify both the size and volume fraction values of the γ″ and γ′ strengthening precipitates in their work [9,12–14].

For the past five decades, a myriad of simplified approaches have been used to characterize the dimensions and volume fractions of γ″ and γ′ precipitates. Early work by Sundaraman et al. [7] utilized dark field transmission electron microscopy (DF-TEM) to image the γ″ and γ′ precipitates and calculated a 4:1 frequency ratio between precipitates by identifying the circular cross-sections as spherical γ′-precipitates and the ellipsoidal cross-sections as γ″-precipitates. The superlattice reflections used for imaging in this work were not cited. However, it is well known that it is challenging to fully distinguish the three DO_{22} variants and $L1_2$ precipitate populations by DF-TEM. This is because all the super-lattice reflections associated with the γ′ precipitates coincide with at least one of the variants of γ″ precipitates; therefore, the γ′ precipitates cannot be isolated using DF-TEM. Furthermore, when the microstructure is imaged on the ⟨001⟩ zone axis, the γ′ and one variant of the γ″ precipitates will appear spherical, leading to further difficulties in separating the two populations through morphology differences.

* Corresponding author at: 21000 Brookpark rd. Mail stop 49-1, Cleveland, OH 44135, United States of America.
E-mail address: timothy.m.smith@nasa.gov (T.M. Smith).

https://doi.org/10.1016/j.matchar.2018.12.018
Received 9 October 2018; Received in revised form 14 December 2018; Accepted 15 December 2018
Available online 19 December 2018
1044-5803/

Future studies have used this 4:1 ratio to calculate volume fraction values, ignoring both the questions on how this ratio was determined or how sensitive the ratio is to composition and heat treatment variations [15,16]. Recent work using high resolution scanning transmission electron microscopy and energy dispersive spectroscopy (STEM-EDS) determined that a volume fraction ratio close to 3:4 [17]. Although this approach lacked stereological considerations and made problematic assumptions such as uniform TEM foil thickness, it highlights that the 4:1 ratio may not be assumed for all heat treated superalloy 718. Bulk x-ray diffraction (XRD) and phase extraction of the minor phases from the matrix [5,12,18,19] are also frequently used to measure precipitate volume fraction; however, neither technique can separate the three different intermetallic precipitates because the crystal structures and compositions are quite similar.

The improvement in resolution for scanning electron microscopy and advancement in image processing techniques have allowed for these three precipitate populations to be accurately separated in a similar way that γ′ strengthened superalloys have been investigated in the past [13,20]. This study presents a new technique that combines scanning electron microscopy (SEM), STEM-EDS and electron backscatter diffraction (EBSD) to rigorously separate the γ″, γ′, and δ precipitates populations to determine the average dimensions, average volume fraction and precipitate size distributions. The average dimensions and volume fraction of the three precipitate populations from this new technique were further validated with bulk XRD and phase extraction measurements on selective laser melted and heat treated samples of superalloy 718.

2. Experimental

2.1. SLM Build/Material/Heat Treatment

A one half inch diameter rod of superalloy 718 was fabricated using SLM at the NASA Marshall Space Flight Center on an Concept Laser M2. The piece was stress relieved at elevated temperature (1066 °C) for 1.5 h under an argon atmosphere before being removed from the plate. The piece was then hot isostatic pressed (HIPed) and homogenized at elevated temperatures [21]. Finally, the sample underwent a conventional heat treatment for superalloy 718 where it was solutionized at 1010 °C for 1 h, gas quenched and followed by a two-step age (718 °C/11 h → 621 °C/6 h) [8]. After post heat-treatment, the sample was cut both longitudinally and transverse from the build direction.

2.2. Etch and Microscopy Methods

For SEM analysis, samples obtained a polished surface by polishing with diamond suspension combined with a final polish using 0.05 colloidal silica and/or diamond paste. To highlight the γ″, γ′ and δ precipitates in the γ matrix, an etchant (which preferentially attacks all three intermetallic precipitates) consisting of 50 mL of lactic acid, 30 mL of nitric acid and 2 mL hydrofluoric acid was applied. The samples were gently swapped with the etchant for about 30 s. Qualitatively, if the γ″ precipitates look as deeply etched as the γ′ precipitates it was considered a satisfactory etch as they were found to etch more slowly than the γ′ precipitates.

For the volume fraction and shape analysis, a high resolution Zeiss Auriga SEM-FIB was utilized using an Everhart-Thornley secondary electron detector with low accelerating voltage (3 kV). Employing low accelerating voltage minimizes the fringe contrast observed around the edges of the etched precipitates thus improving image post processing [13]. EBSD orientation mapping was performed using an EDAX Hikari EBSD detector to identify the ⟨001⟩ and ⟨111⟩ oriented grains used for this analysis. For this study, mis-orientation angles never exceeded 3° from the desired orientation. EBSD data was collected using the TSL OIM Data Collection 7 software and was analyzed using the TSL OIM Analyzer software.

For morphology measurements (i.e., determining the cut-off aspect ratio for the SEM analysis) STEM-EDS was performed using a FEI Talos STEM at 200 kV. For this analysis, 3 mm disks where extracted from the SLM bar using electrical discharge machining (EDM). These disks were then polished down to about a 150 μm thickness using 600 and 800 grit SiC polishing pads and subsequently electropolished using a Struers twin-jet unit at −40 °C using 10.5 V in a solution of 20% perchloric acid and 80% methanol. The EDS maps were acquired using Super-x EDS detectors and Bruker VELOS software which has active drift correction. The Super-X EDX detection system utilizes two silicon drift detectors around the objective pole piece for improved collection performance. Maps were obtained using experimental K_α energies for Ni, Al, Cr, Ti, Fe, Co and L_α energies for Nb and Mo [22].

2.3. XRD Analysis

A mounted piece of SLM 718 sample was analyzed with a Panalytical Empyrean x-ray diffractometer using a position sensitive detector (Galipix) in scanning 1D mode. Because of the relatively large grain size of the matrix phase (estimated average grain diameters are about 50 μm from EBSD analysis), multiple measurements were taken to increase crystallite statistics. Mo Kα radiation was used to increase the effective sampling volume (vs. Cu Kα). Although this doubled the beam penetration into the sample as compared to Cu Kα (13 μm vs. 6 μm for 99% contribution to the diffracted beam at the 100% peak of the matrix phase, d = 2.08 Å), the penetration depth was still significantly less than the typical diameter of a matrix grain. Secondly, the sample was rotated about the axis perpendicular to the sample surface during acquisition to bring more grains into the diffracting condition. A wobbled scan was performed for each sample run. This consisted of 9 individual scans in which the goniometer ω-offset was varied by ± 2° in 0.5° increments. Seven sample runs were performed with serial polishing steps between each run in which ~100 μm of the top surface were removed to expose new grains. The scans underwent quantitative phase analysis (QPA) using whole pattern fitting (WPF) as implemented in the Jade analysis program. Crystal structures from the Powder Diffraction File (PDF-4 + 2015) were modified to reflect the known chemical composition of the IN718 phases [23].

3. Results

3.1. SEM and EBSD Characterization

It has been well documented that the γ″ strengthening precipitates form circular platelets along all three {001} crystallographic planes [9,16,17]. As a result of this crystallographic relationship, if the γ″ platelets are imaged using an SEM from an ⟨111⟩ oriented grain, as displayed in Fig. 1(c), all three variants of the γ″ precipitates will acquire a “cigar-like” ellipse morphology. Consequently, from this orientation the “circular-like” γ′ precipitates are more easily separated from the “cigar-like” γ″ precipitates. If the precipitates are imaged from an ⟨001⟩ oriented grain, as shown in Fig. 1(d), two out of the three variants of the γ″ precipitate can be imaged edge-on. Thereby eliminating the need for more complicated stereological considerations for size analysis of the precipitates (refer to Section 3.4) Thus, separate size dimensions and volume fraction characteristics can be determined between the intergranular γ′ and γ″ precipitates. With respect to imaging the specific oriented grains, an EBSD map was performed and the closest ⟨001⟩ and ⟨111⟩ grains were selected from the map for later SEM analysis. The EBSD map used for this analysis is shown below in Fig. 1(a).

Fig. 1(a) shows the grain structure and equiaxed texture of the SLM 718 after post processing. To find the selected grains in the EBSD map, a single fiducial marker “+” was etched into the sample using an ion beam at high current (16 nA). Fig. 1(b) represents the orientation of the two grains selected and the corresponding precipitate microstructure of

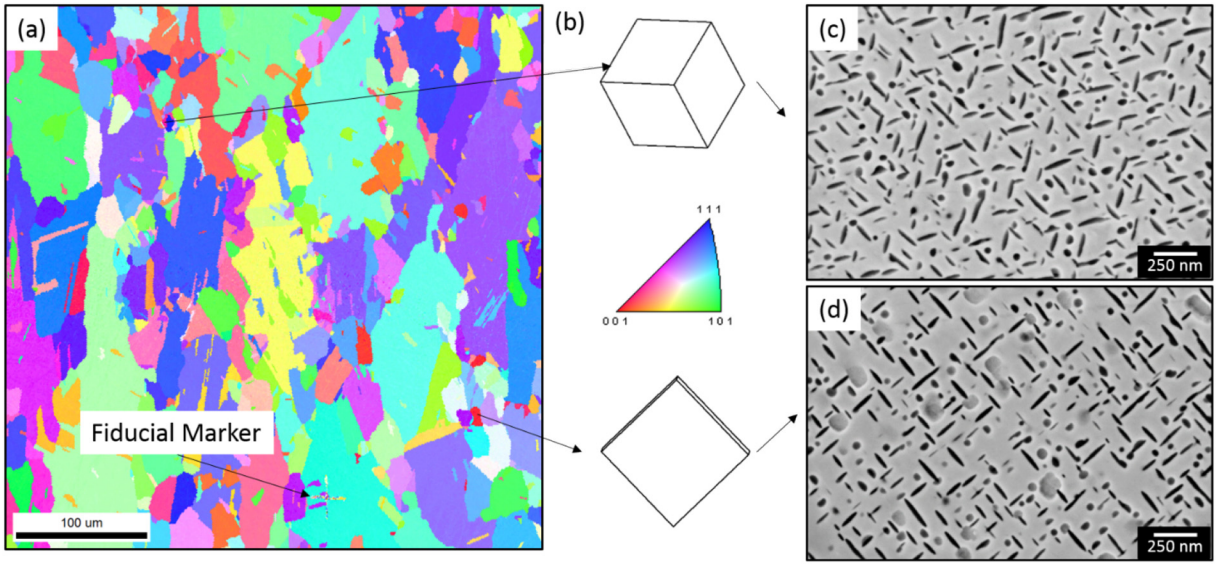

Fig. 1. An EBSD map revealing an (b) ⟨111⟩ and ⟨001⟩ oriented grain near the fiducial marker. On the right: the corresponding low kV SEM images of the etched surface from the (c) ⟨111⟩ oriented grain and the (d) ⟨001⟩ oriented grain.

each grain are presented in Fig. 1(c), which shows the ⟨111⟩ oriented grain and Fig. 1(d) which presents the ⟨001⟩ oriented grain. In the ⟨111⟩ oriented grain (Fig. 1c) all three variants of the "cigar-like" shaped γ″ precipitates can be observed, rotated 120° from each other. Whereas the γ′ precipitates all appear circular. The ⟨001⟩ oriented grain reveals the two γ″ variants edge-on while the third variant is viewed parallel to the sample surface and appear as large, lightly etched circular features. From the ⟨001⟩ oriented SEM images, it is impossible to separate the γ′ and γ″ precipitates because one γ″ variant and the γ′ precipitates both appears circular. Therefore, as was stated earlier, volume fraction analysis must be performed using the ⟨111⟩ oriented SEM images as all three variants of the γ″ precipitates can be separated from the γ′ precipitates through their morphology (i.e., aspect ratios).

3.2. STEM-EDX Analysis – Quantified Precipitate Morphology

Another characteristic that differs between the γ′(Ni_3Al,Nb) and γ″(Ni_3Nb) precipitates is their chemistry (albeit only slightly) where Aluminum preferentially partitions to the γ′ precipitates and Niobium to the γ″ precipitates. High resolution STEM-EDS mapping in Fig. 2 shows the preferential partitioning of these elements to the two precipitates.

Fig. 2(a) reveals a high angle annular dark field (HAADF-STEM) image of the microstructure near a ⟨111⟩ zone axis. A combined Al and Nb elemental maps from the same area is shown in Fig. 2(b). The Nb (green) enriched areas highlight the γ″ precipitates while the Al (red) enriched areas highlight the γ′ precipitates. Ti was found to segregate to both precipitates almost equally and therefore was excluded in this analysis. From Fig. 2(b), the two strengthening precipitates, γ″ and γ′, can be separated by their respective chemistries, as a result, their shape can be quantified. The aspect ratios of each individual precipitate was measured and are shown in Fig. 3.

Fig. 3 reveals a density map that shows overlap between the aspect ratios of the two precipitate populations. As has been assumed in earlier literature [16,17], the precipitate microstructures are best characterized near ⟨111⟩ orientations because all three $D0_{22}$ variants of γ″ are elongated in this plane, while γ′ are spherical allowing unique identification by the aspect ratios. To separate these populations, an optimal cut-off value of 2.25 aspect ratio is identified for this case, as this value will vary with differing chemistry and heat treatment paths. The cut-off value was selected by obtaining approximately equal frequency of γ′-precipitates above and γ″-precipitates below the cut-off value such that these frequencies cancel each other in the overall measurement. To examine the accuracy of using the 2.25 aspect ratio cutoff, area fractions from the EDS image in Fig. 2b were determined two ways; using the Al and Nb chemical segregation to segment the precipitates (actual) vs separating the precipitates using the aspect ratio cutoff (measured). By using the 2.25 aspect ratio as a cut-off value, the area fractions were

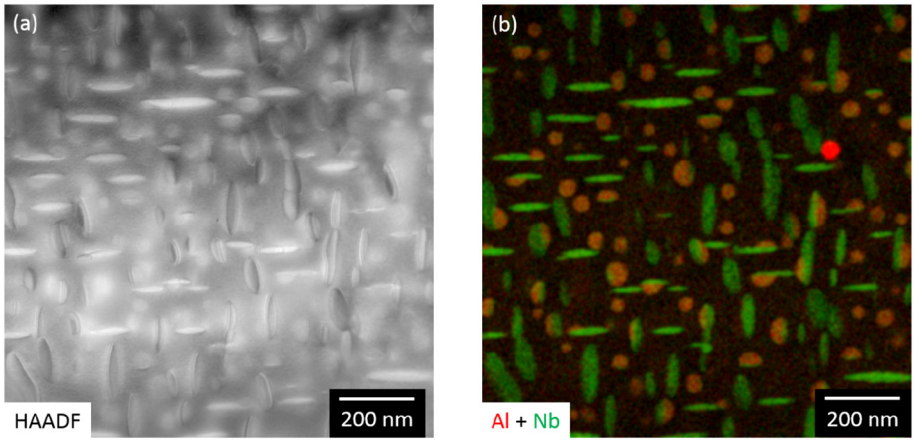

Fig. 2. (a) A HAADF-STEM image of superalloy 718. (b) A combined elemental Nb and Al map of the same area revealing γ″ and γ′ precipitates from super X-EDS. Al (red) corresponds with the γ′ precipitates while Nb (green) corresponds with the γ″ precipitates. (For interpretation of the references to color in this figure legend, the reader is referred to the web version of this article.)

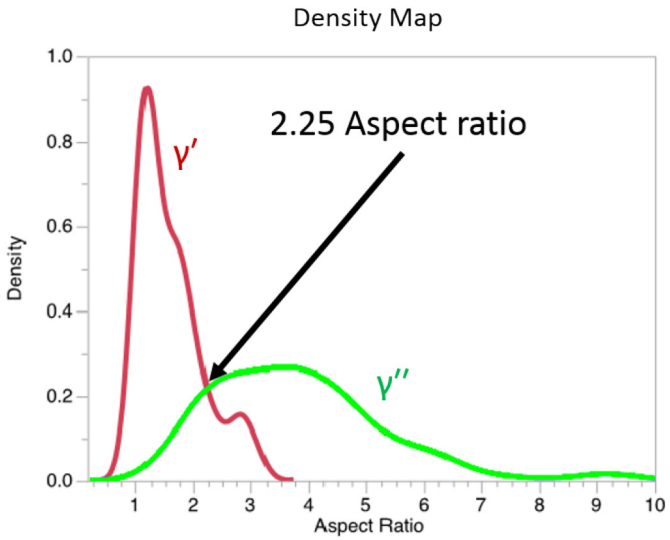

Fig. 3. A density map reveals that using an aspect ratio of 2.25 will work the best to separate the precipitates.

found to be within error of the actual area fraction percentages, (γ″ actual: 13.2% vs. measured: 13.1% and γ′ actual: 5.8% vs. measured: 5.9%). The slight discrepancy between the two values most likely arises from assuming equal particle sizes near the cutoff aspect ratio when this isn't entirely accurate in practice.

3.3. SEM Image Post-processing

For the two populations delineated by the 2.25 cut-off value, the dimensions, number density and volume fraction were measured from the multiple, etched SEM images. Still, artifacts from acquiring images at high magnifications may alter the actual characteristics. These scan and vibration distortions were removed using code developed by Ophus et al. [24] and the process is described below in Fig. 4.

Fig. 4(a) reveals a raw image of the etched surface of a ⟨111⟩ oriented grain, taken at high magnifications (> 100kx). By acquiring another image of the same area with a 90° scan rotation from the first (Fig. 4(b)) the MathWorks MATLAB® code can produce an image where all horizontal scan vibrations are removed (Fig. 4(c)) [24]. The difference between the original and corrected images is highlighted in Fig. 4(d) and Fig. 4(e). Many of the visible distortions have been removed thus producing a more accurate representation of the precipitate microstructure. This step was performed for all images analyzed in this study. Fig. 5, presents the image post-processing steps taken to manually separate the intergranular γ″ and γ′ precipitates.

Fig. 5(a) shows a representative scan corrected etched SEM image of the SLM 718 surface. Using the adaptive threshold ImageJ plug-in the image can be accurately segmented via gray-scale contrast between the etched precipitates and the lighter unetched γ matrix, as shown in Fig. 5(b) [25]. The adaptive threshold plug-in determines a gray-scale cut-off as well as the minimum dimension of the precipitate. Hence, any pixel that is determined "dark" enough to be considered a precipitate must also have a minimum number of 8 connecting "dark" pixels for it to be considered a precipitate and included in the thresholding step. Otherwise, the plug-in will consider that pixel as noise and exclude it. Some γ′ particles precipitated off of γ″ precipitates creating a composite particle of the two types. These composite particles were previously discovered by Phillips et al. [26] using near atomic resolution EDS. Consequently, a preliminary watershed was performed on the segmented images and completed by hand using ImageJ as shown in Fig. 5(c). The γ′ precipitates were then separated from the γ″ precipitates using the BioVoxxel plug-in for ImageJ and the cutoff aspect ratio determined in Fig. 3(b) [27]. The particles representing γ′ precipitates, with an aspect ratio under 2.25, are highlighted in Fig. 5(d) while the γ″ precipitates, with an aspect ratio > 2.25, are represented in Fig. 5(e). Finally, a composite image representing the SLM 718 microstructure is produced as shown in Fig. 5(f). From this image, the area fraction amounts of each precipitate can be calculated, as well as the dimensions of the γ′ precipitates. For the γ″ precipitates, the same procedure was employed using the ⟨001⟩ oriented SEM images, which excludes the one γ″ variant not imaged edge-on and the γ′ precipitates. The same procedure, using low magnification SEM images, was also employed to calculate the volume fraction of the delta phase. Fig. 6 shows a representative image processing for the δ precipitates.

In a similar fashion, morphology was used to separate the delta

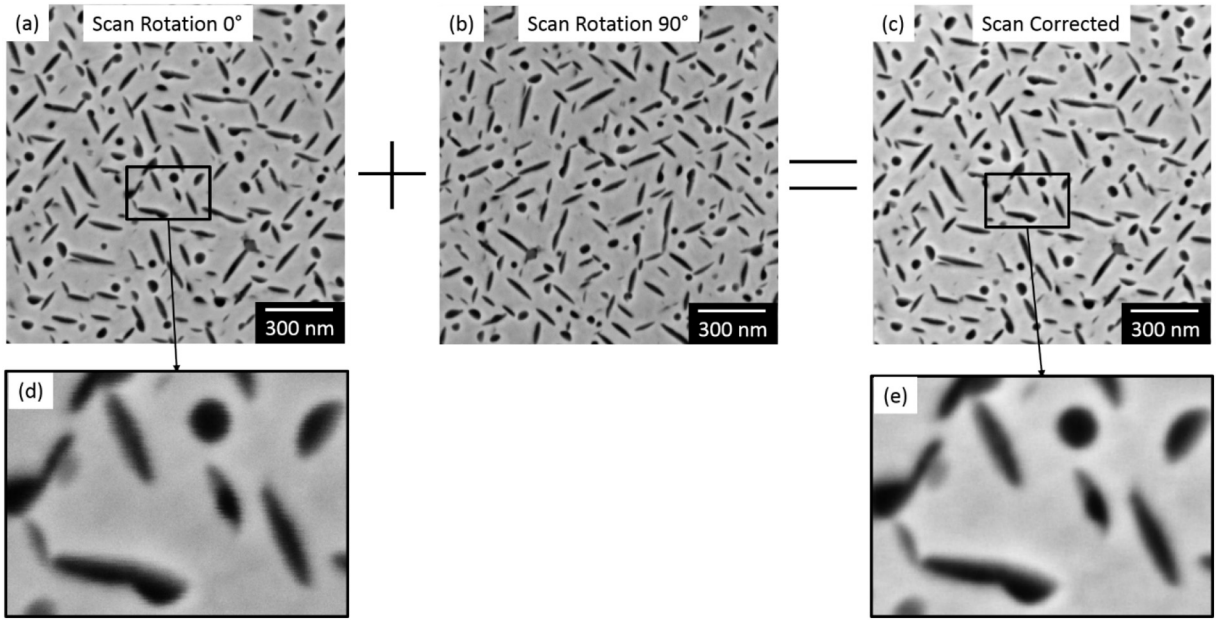

Fig. 4. An original SEM image of area (a) and a 90° rotated scan of the same area (b) were used to create a scan distortion corrected image (c). (d) Represents the scan distortions common for micrographs taken at high magnifications while (e) shows the same area after the distortion have been corrected following the code developed by Ophus et al. [24].

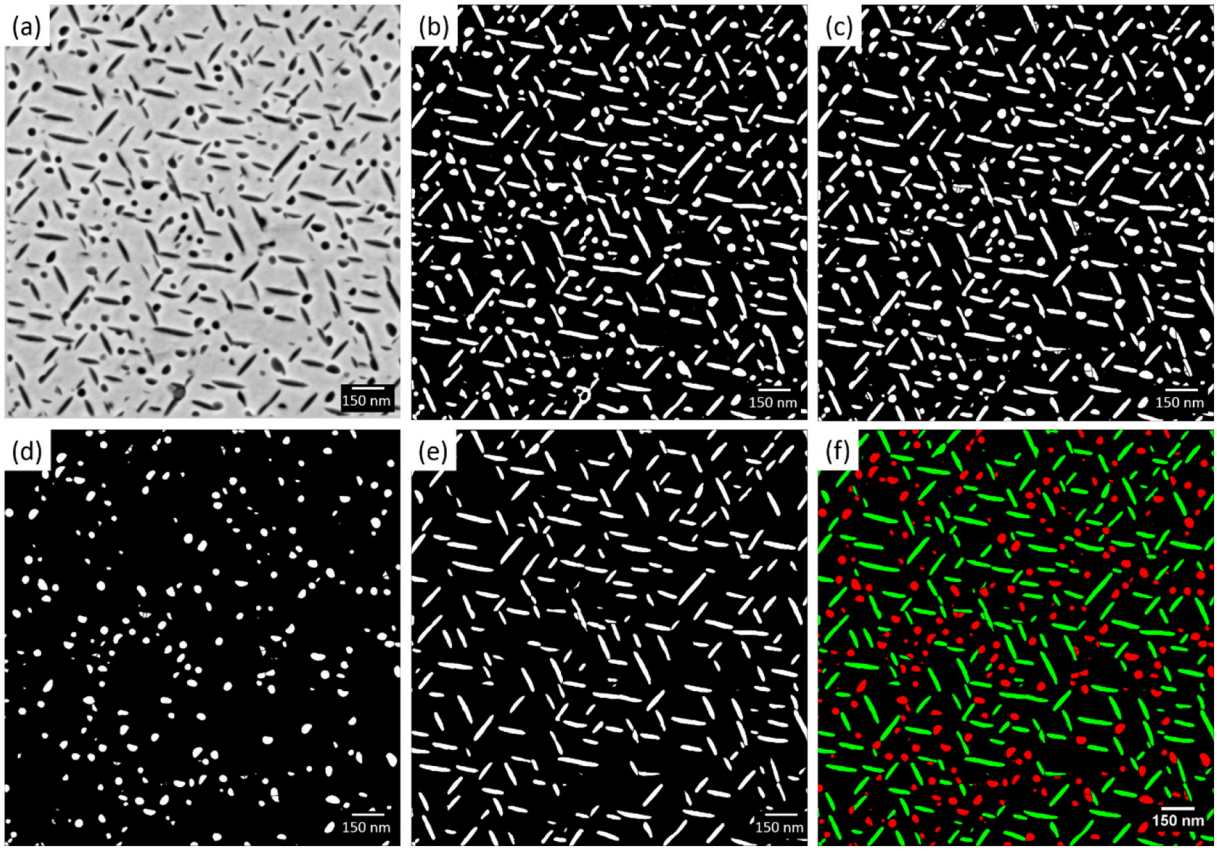

Fig. 5. (a) An etched surface of superalloy 718 using a secondary detector with low kV. (b) The etched precipitates are highlighted using adaptive threshold plugin in ImageJ. (c) The precipitates are then separated using a watershed algorithm with some manual clean up. The precipitates are then separated using the aspect ratio determined from EDS. (d) Shows the γ′ precipitates and (e) shows the γ″ precipitates. (f) Finally, a composite image can be created showing the microstructure on the superalloy.

phase needles and the blocky MC-carbides along grain boundaries. This difference in morphology between the grain boundary phases was confirmed through STEM-EDS by the partition of Ti to the MC carbides and Ni to the δ precipitates, as shown in Fig. 7.

3.4. Automated SEM Image Post-processing

The previously described segmentation steps are cumbersome, prone to human interpretation and ineffective as a method of quantifying the fraction of γ′ and γ″ precipitates for a materials processing study. A more robust, high-throughput manner is necessary to develop a model and optimize SLM processing parameters. An automated image processing algorithm was developed to accurately and efficiently separate the γ′ and γ″ precipitates in the SEM micrographs. The algorithm was written in Python (v2.7) using NumPy, Matplotlib, Skimage, Opencv, Pylab, Math, and Scipy libraries; the individual modules are indicated in parentheticals as necessary. The algorithm, based on the approach of Zafari et al. [28], automates the identification and segmentation of γ′ and γ″ phases from grayscale secondary electron images, including the particles that co-precipitated.

Fig. 8(a) shows a representative secondary electron micrograph of an etched SLM 718 surface. In order to threshold the precipitates from the unetched matrix, an Otsu threshold filter (skimage.filters.threshold_otsu) was performed to identify the etched precipitates from the lighter unetched γ matrix, generating a b/w binary image. This was followed by a morphology filter (skimage.remove_small_objects) which

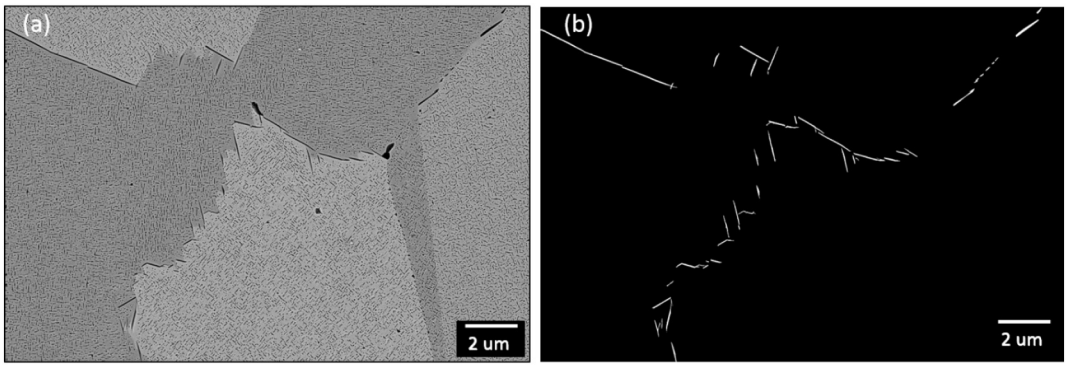

Fig. 6. (a) Low kV SEM image highlighting the etched δ precipitates and carbides along grain boundaries. Morphology differences were used to label carbides (blocky) and δ precipitates (needle-like). (b) The segmented image revealing the δ precipitates.

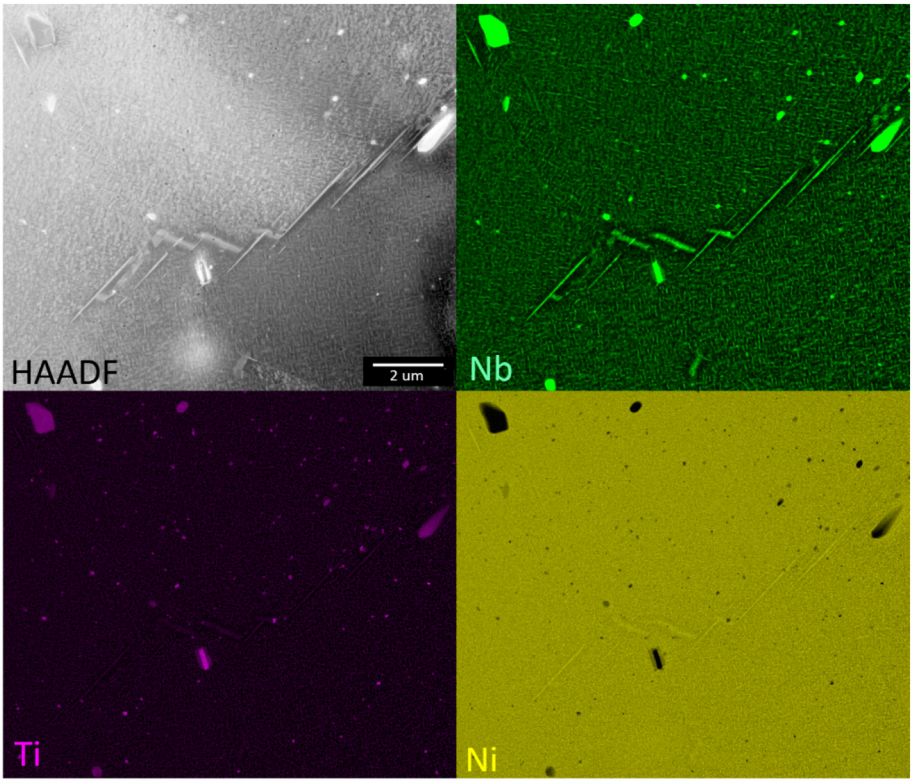

Fig. 7. HAADF-STEM, Nb, Ti, and Ni elemental maps of a SLM 718 grain boundary highlighting the Nb/Ni rich needle-like δ phase along with Ti and Nb rich globular carbides.

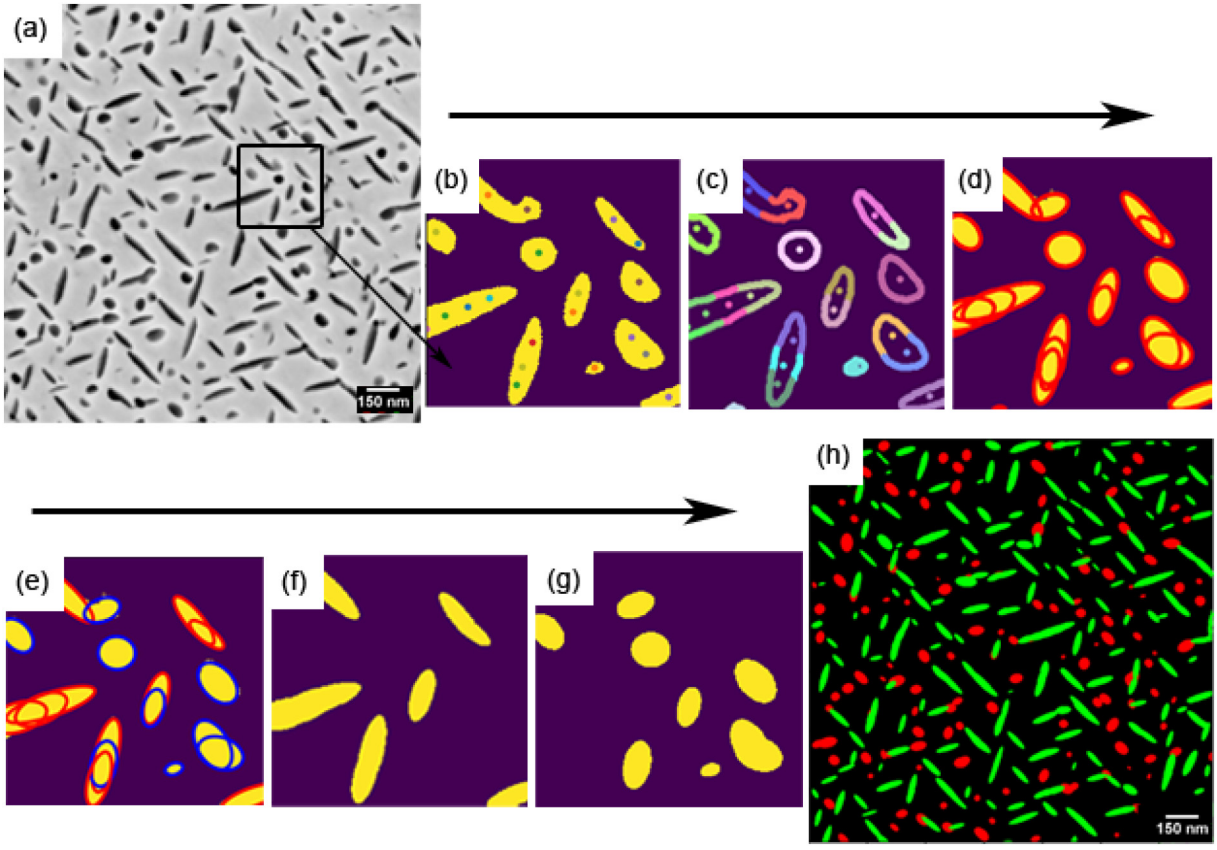

Fig. 8. (a) An etched surface of superalloy 718 using a secondary detector with low kV. (b) Seed-point extraction (c) association of the edge-points to the seed-points. (d) Prediction of contours using classical ellipse fitting. (e) The precipitates are then separated using the aspect ratio determined from EDS. (f) Shows the γ″ precipitates and (g) shows the γ′ precipitates. (h) Finally, a composite image can be created showing the microstructure on the superalloy.

removed the noise from the image. To improve the identification and separation of the individual precipitates, a two iteration erosion operation (skimage.morphology.erosion) was then performed.

After the preprocessing, fast radial symmetry (FRS) transformation [29] calculates the presence and number of individual objects as seed-points as shown in Fig. 8(b). Scharr transformation (skimage.-filters.scharr) and skeletonization (skimage.morphology.skeletonize) were used to identify the edge-points. After seed-point detection, a correlation matrix between edge-points and seed-points was generated based on the distance and divergence between the seed-points and the edge-points [30]; The smaller the distance and divergence between a seed point and edge point indicates a higher correlation. These correlation values are then used to assign each group of adjacent edge-points (called a contour) with a seed-point based on highest relevance, as shown in Fig. 8(c). Classical ellipse fitting [31], which finds the optimized ellipse based on the given seed-point and associated contour, was used to complete a contour around the seed-point – representing individual precipitates, shown in Fig. 8(d).

The γ′ precipitates were then differentiated from the γ″ precipitates based on the 2.25 cutoff aspect ratio determined in Fig. 3(b) as shown in Fig. 8(e) [23]. For image processing, aspect ratios for each particle were calculated by fitting a minimum sized rectangle that circumscribes the ellipse (shapely.geometry.polygon). The major axis of the ellipse was calculated as the length of the rectangle. The particles representing γ″ precipitates (aspect ratio $>$ 2.25), are visualized in Fig. 8(f) while the γ′ precipitates, with an aspect ratio $<$ 2.25, are visualized in Fig. 8(g). Finally, a composite image representing the co-precipitated superalloy 718 microstructure is visualized in Fig. 8(h). The algorithm chooses the γ″ (green) over the γ′ (red) whenever their contours overlap. This step accurately separates the composite γ′/γ″ particles that needed to be individually performed in the manual segmentation approach. From the final composite image both volume fraction and size distributions can be calculated.

3.5. Volume Fraction and Size Analysis

For the area fraction calculation, all the pixels of each type of precipitates are counted and divided by the area of the image. Table 1 presents the measured area fractions for the γ″, γ′, and δ phases along with the standard deviation errors for both the manual and automated segmentation processes.

The results in Table 1 are significant in that they reveal statistically equivalent area fractions (within error) of the γ′ and γ″ precipitates between the automated and manual segmentation techniques. Another observation was that both procedures reject the 4:1 γ″/γ′ volume fraction ratio assumed is past work [15]. This difference may reveal that precipitate characteristics in superalloy 718 are considerably sensitive to the subtle chemistry and heat treatment differences inherent in superalloy 718 processing. The volumetric and size distributions of the γ′ and γ″ precipitates as calculated by spherical-equivalent diameters are presented in Fig. 9 and Fig. 10, respectively for both the manual and automated techniques.

Again, both methods (manual and automated) produced comparable number density curves. To determine the volumetric size distributions, the area size distributions were measured for all γ′ and the γ″ precipitates. The ⟨111⟩ oriented images were used for the γ′ size analysis and the ⟨001⟩ oriented images were used for the γ″ size analysis. By only using the two variants of γ″ precipitates that are edge-on, their spherical-equivalent diameters can be calculated using the same relationships employed for the γ′ precipitates [32]. The numerical volumetric size distributions were calculated from the measured area size distributions assuming a spherical precipitate morphology by using [33]:

$$(N_v)_j = \frac{1}{\Lambda}\sum_{i=j}^{k} \alpha_i (N_A)_i \quad (1)$$

where N_A is the experimentally obtained area number densities,

Table 1
Area fraction measurements of the three intermetallic phases in an SLM 718 as determined by the described SEM imaged process analysis. Also presented is the γ″/γ′ area fraction ratio.

Precipitate	Manual (%)	Auto (%)
γ′	5.1 ± 0.8	5.1 ± 0.4
γ″	11.1 ± 0.9	11.5 ± 0.4
γ″:γ′	2.18:1	2.25:1
δ	0.37 ± 0.24	N/A

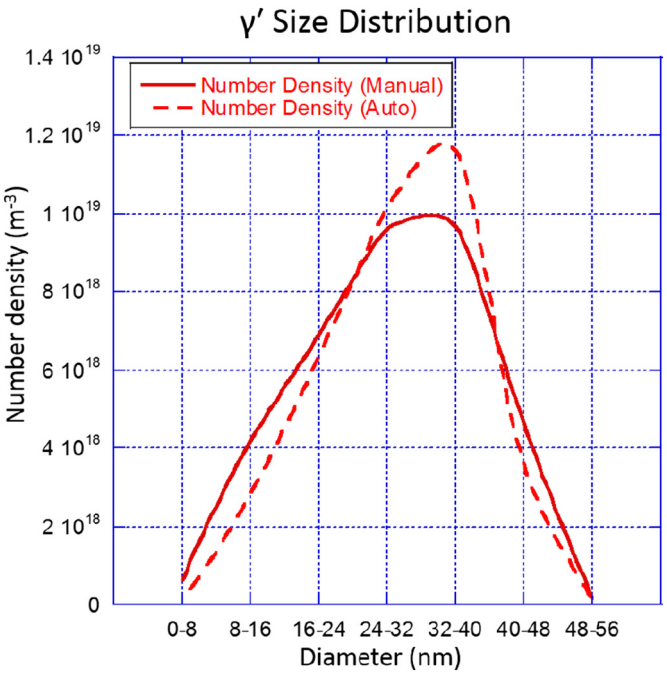

Fig. 9. Volumetric size distributions of the γ′ precipitates in the superalloy 718 sample as determined using the manual and automated segmentation procedures.

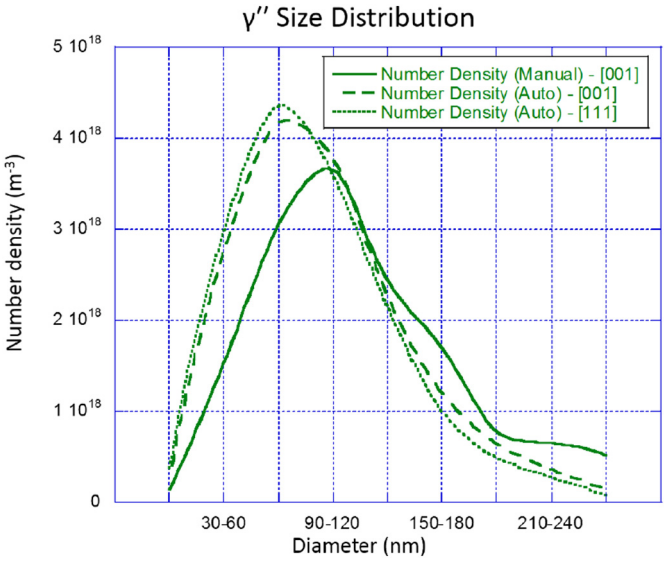

Fig. 10. Volumetric size distributions of the γ″ precipitates in the superalloy 718 sample as determined using the manual and automated segmentation procedures.

$D_{max} = k\Delta$, and k equals the total number of size groups. The value for α is a pre-determined set of coefficients associated with the probability of the polish surface plane cutting a sphere acquired by systematically calculating the values of $P_{i,j}$ for all class intervals [33].

$$P_{i,j} = \frac{1}{r_{max}}\left[\sqrt{(r_{max}{}^2) - (r_{i-1})^2} - \sqrt{(r_{max}{}^2) - (r_i)^2}\right] \quad (2)$$

Interestingly, unlike the γ′ precipitates which presented a normal size distribution, the γ″ precipitates present a log-normal size distribution, this may be due to preferential diffusion along elastically soft directions of non-spherical geometries. In addition, there did not appear to be a significant difference between the size distributions of the γ″ precipitates imaged in the ⟨001⟩ and ⟨111⟩ oriented grains. Therefore, in future studies it may be sufficient to calculate size distributions for both the γ′ and γ″ precipitates using the ⟨111⟩ oriented grains exclusively. Regardless, future work is still needed to determine how nucleation and precipitation of these phases may affect the size distributions of these precipitates.

4. Discussion

4.1. Stereology Considerations

One goal of this study is to accurately determine the volume fractions of the three intermetallic precipitates in the SLM 718 sample. In order to convert the area fraction values to volume fraction, consideration must be given towards the interaction volume associated with the SEM images. If sub-surface precipitates are imaged and calculated in this procedure, then a correction factor must be applied to the area fraction numbers. The Monte Carlo simulation program, CASINO [34], was employed to determine the interaction volume of backscattered electrons under the microscope parameters used for the above analysis. The results are shown below in Fig. 11.

A simulation of over 100,000 electrons was performed and the backscattered electron (BSE) penetration depth of 1000 of those electrons was measured as shown in Fig. 11. The BSE's that were able to escape never penetrated further than 30 nm into the 718 sample, with the majority only interacting with the first 15 nm of the sample.

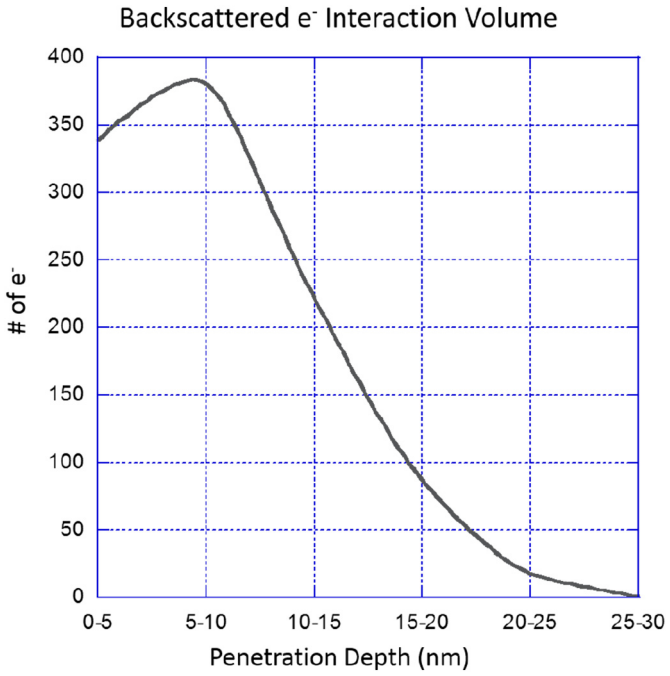

Fig. 11. The penetration depths of escaped backscattered electrons produced by a 3KeV source, modelled using CASINO.

Unfortunately, CASINO cannot calculate the interaction volume of the secondary electrons, nevertheless, considering that it has been well established that interactive secondary electrons penetrate a sample an order of magnitude less than BSE's, it is likely that the secondary electron interaction volume used for this analysis only penetrated a few nanometers into the sample [35,36]. In addition, the contrast from the Everhart-Thornley detector is from surface topological differences and not chemical (Z-contrast) differences as would be observed when imaging with back-scattered electrons [35]. As a result, even if a sub-surface precipitate was imaged almost no contrast would be observed and the precipitate would be removed as noise during the thresholding step. Hence, the etched SEM images can be assumed as a true two-dimensional cross-section representation of the sample volume. By making a true section of the sample through this SEM technique described above, a one-to-one relationship between volume and area fractions of the precipitates (i.e., $V_V = A_A$) holds true for particles of any shape or size, including when there may be a distribution of sizes [32,37–39]. From this relationship, the measured area fractions of the γ″, γ′, and δ phases represent their respective volume fractions as well.

4.2. Validation Through Phase Extraction Analysis and XRD

In order to validate the calculated volume fractions of the three precipitates determined from the SEM images of the SLM 718 sample, more conventional approaches of phase extraction and XRD were performed. For the phase extraction analysis, an approximate 1 × 1 × 1 cm sample was cut from the SLM 718 bar weighing 4.53 g. The precipitates were extracted using a 1% ammonium sulfate, 1% citric acid electrolyte at a current density of 100 mA/cm^2 for 1 h [40]. Due to the chemical similarities between the three intermetallic phases (γ″, γ′, and δ), the phase extraction solution could only measure the combined overall weight fraction of the three precipitate types. The combined weight percent value of the three precipitates was converted to a combined volume fraction using conventional compositional conversion principles and assuming a linear rule of mixtures approximation for two phases (i.e., precipitate and matrix) [40]. The combined volume fraction for all three phases (γ″, γ′, δ) was determined to be 15.7%.

To acquire separate precipitate volume fraction quantities from the overall volume fraction value obtained using phase extraction, bulk XRD was performed on a mounted piece of the SLM 718 sample. Fig. 12 shows the spectrum for the γ/γ′, γ″, NbC, and δ phases determined from this bulk XRD analysis.

The γ and γ′ phases were considered together due to the low γ′ volume fraction and size resulting in the suppression of the γ′ superlattice peaks. For the γ″, γ′, and δ phases, the Ni, Cr, Fe, and Mo atoms were assumed to be entirely located on Ni sites, whereas the Al, Nb, Ta, and Ti were assumed to be located entirely on Al/Nb sites. To improve accuracy, preferred orientation models that utilize a minimization of the fitting residuals and use spherical harmonics were applied to the XRD spectra. However, it is entirely possible that poor crystallite statistics, from the large average grain diameters (> 40 μm), are at the cause of fitting deviations rather than preferred orientation.

The error bars for the measured volume fractions and lattice parameters in Table 2 represent one estimated standard deviation (esd) as calculated by the XRD analysis program. It should be noted that these error values do not represent the full possible error, but rather give a standard statistical error regarding the fit of the model parameters to the data. Again, the γ′ precipitates could not be measured because the visible peaks could not be distinguished from the γ phase due to similar crystal structures and nearly identical lattice parameters. Thus, only the γ″ and δ phases could be analyzed. From the XRD analysis, the measured γ″ volume fraction was 10.6%. This is very close and within error bars to the 11.1–11.5% determined from the SEM analysis. No δ phase was measured by XRD, most likely due to the small amount present (0.37% determined from SEM images) in the sample. These results, combined with the phase extraction work, produce estimated volume

Phase ID (4)	Chemical Formula	PDF-#	Space Group	Vol% (esd)	Wt% (esd)	a (esd)	c (esd)
γ/γ'	IN_{718}	98-000-1033	cFm-3m (225)	89.34 (3.11)	88.30 (2.26)	3.59588 (17)	3.59588 (17)
γ''	IN_{718}	98-000-1036	tI4/mmm (139)	10.57 (0.63)	11.62 (0.63)	3.61425 (63)	7.42937 (132)
NbC	NbC	04-001-1554	cFm-3m (225)	0.09 (0.02)	0.09 (0.02)	4.43000 (0)	4.43000 (0)
δ	IN_{718}	98-000-1035	oPmmn² (59)	0.00 (0.00)	0.00 (0.00)	5.14100 (0)	4.53400 (0)

Refinement Halted (R/E=13.92), ♣ Round=4, Iter=6, P=31, R=9.0% (E=0.65%, EPS=0.5)

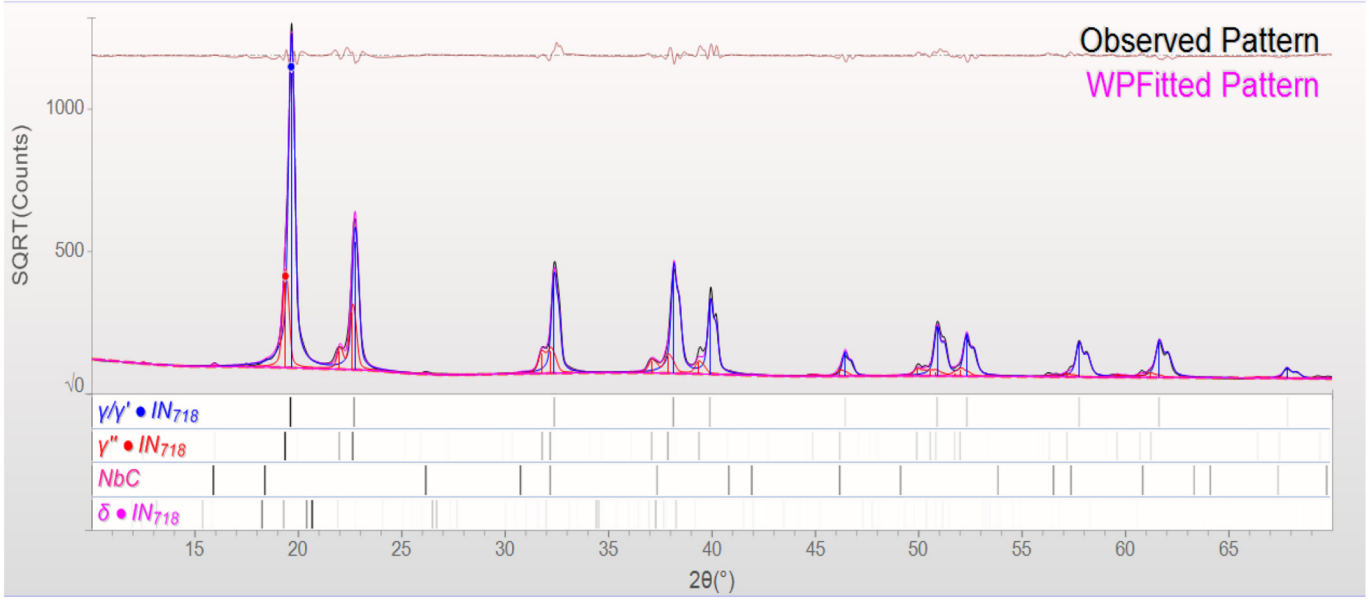

Fig. 12. XRD data and QPA analysis results. The XRD scan is the sum of the data from all 7 serial sections.

fractions of the three strengthening phases. Table 2 below compares these results with the volume fractions measured previously using the SEM analysis.

The combined XRD and phase extraction analysis clearly validate the measured volume fraction values from the SEM analysis. Indeed, the SEM analysis may be more accurate as visual confirmation of the measurements can be performed while errors associated the XRD and phase extraction methods are, in many cases, unknown to the researchers. For example, the XRD and phase extraction techniques failed to measure the presence of any δ phase, which was previously shown in both Fig. 6 and Fig. 7, to exist along grain boundaries in the sample. Therefore, this novel SEM characterization method described throughout this paper offers the advantage that low volume fraction and nano-scale phases are detectable.

5. Conclusions

This study investigated the volume fraction and size distributions of the three strengthening precipitates (γ″, γ′, and δ) through a new low kV SEM technique, which also incorporated high resolution STEM-EDX. The new technique was found to be a more robust and accurate microstructure characterization method for Superalloy 718 and refutes many of the assumptions made in previous studies. The following conclusions can be drawn.

(i) Monte Carlo simulations confirm that low kV (3 kV) SEM analysis using an Everhart-Thornley detector removes the interaction of sub-surface precipitates allowing for true 2-D cross-sectional images to be acquired.
(ii) STEM-EDS analysis confirms the presence of composite γ′/γ″ particles.
(iii) The volume fraction ratio between γ″ and γ′ precipitates was found to be near 2:1. While the ratio of volumetric number density was near 1:10.
(iv) The automated segmentation code accurately separates the γ′ and γ″ precipitates in the SEM images and provide volume fraction and size distributions of each precipitate type.
(v) γ′ precipitates displayed a normal size distribution while the γ″ precipitates were found to possess a log-normal size distribution.
(vi) Conventional XRD and phase extraction techniques confirm the precipitate volume fraction results obtained utilizing high resolution SEM.

In combination, the characterization procedure described throughout this study has been validated by conventional methods. These new techniques will allow for insights into the nucleation and growth of these nano-scale strengthening precipitates and improve the validation of future CALPHAD precipitation models.

Acknowledgements

TMS would like to acknowledge the NASA Human Exploration and

Table 2
Volume fraction measurements of three intermetallic phases in an SLM 718 from the SEM analysis compared to the XRD and phase extraction experiments.

Precipitate	SEM analysis (manual)	SEM analysis (auto)	XRD	Phase extraction	Phase extraction and XRD
γ′	5.1 ± 0.8%	5.1 ± 0.4%	N/A	15.7%	5.1 ± 0.6%
γ″	11.1 ± 0.9%	11.5 ± 0.4%	10.6 ± 0.6%		10.6 ± 0.6%
δ	0.37 ± 0.24%	0.37 ± 0.24%	0%		0%

Operations Mission Directorate (HEOMD) Space Launch System Liquid Engine Office Project for funding this study under the Additive Manufacturing Structural Integrity Initiative project. TMS also acknowledges Dereck Johnson (NASA-GRC) for his help with the phase extraction experiment. The contribution of the co-authors at Case Western Reserve University was based upon work supported by the National Science Foundation under Grant No 1152716.

Data Availability

The data required to reproduce these findings is available to download from https://github.com/CWRU-MSL/GammaDoublePrime and/or is available from the corresponding author upon request.

References

[1] K. Amato, S.M. Gaytan, L. Murr, E. Martinez, P. Shindo, J. Hernandez, S. Collins, F. Medina, Microstructure and mechanical behavior of Inconel 718 fabricated by selective laser melting, Acta Mater. 60 (2012) 2229–2239.
[2] A. Strondl, M. Palm, J. Gnauk, G. Frommeyer, Microstructure and mechanical properties of nickel based superalloy IN718 produced by rapid prototyping with electron beam melting (EBM), Mater. Sci. Technol. 27 (2011) 876–883.
[3] L. Parimi, G.A. Ravi, D. Clark, M.M. Attallah, Microstructural and texture development in direct laser fabricated IN718, Mater. Charact. 89 (2014) 102–111.
[4] J.M. Oblak, D.F. Paulonis, D.S. Duvall, Precipitates, coherency strengthening in Ni base alloys hardened by DO_{22}, Metall. Trans. 5 (1974) 143–153.
[5] J.W. Brooks, P.J. Bridges, Metallurgical stability of Inconel alloy 718, Superalloys 1988 (1988) 33–42.
[6] R. Cozar, A. Pineau, Morphology of γ′ and γ″ precipitates and thermal stability of Inconel 718 type alloys, Metall. Trans. 4 (1973).
[7] M. Sundararaman, P. Mukhopadhyay, S. Banerjee, Deformation behaviour of g″ strengthened Inconel 718, Acta Metall. 36 (1988) 847–864.
[8] SAE, AMS5664F, (2017).
[9] B. Dubiel, A. Kruk, E. Stepniowska, G. Cempura, D. Geiger, P. Formanek, J. Hernandez, P. Midgley, A. Czyrska-Filemonowicz, TEM, HRTEM, electron holography and electron tomography studies of γ and γ nanoparticles in Inconel 718 superalloy, J. Microsc. 236 (2009) 149–157, https://doi.org/10.1111/j.1365-2818.2009.03283.x.
[10] R.B. Li, M. Yao, W.C. Lui, X.C. He, Isolation and determination for d, c 0 and c 00 phases in Inconel 718 alloy, Scr. Mater. 46 (2002) 635–638.
[11] K. Kulawik, P.A. Buffat, A. Kruk, A.M. Wusatowska-Sarnek, A. Czyrska-Filemonowicz, Materials Characterization Imaging and characterization of γ′ and γ″ nanoparticles in Inconel 718 by EDX elemental mapping and FIB – SEM tomography, Mater. Charact. 100 (2015) 74–80, https://doi.org/10.1016/j.matchar.2014.12.012.
[12] X. Xie, J. Dong, G. Wang, W. You, The effect of Nb, Ti, Al on precipitation and strengthening behavior of 718 type superalloys, Superalloys 718, 625, 706 Var. Deriv. 3, 2005, pp. 287–298.
[13] P.M. Sarosi, G.B. Viswanathan, D. Whitis, M.J. Mills, Imaging and characterization of fine gamma prime precipitates in a commercial nickel-base superalloy, Ultramicroscopy 103 (2005) 83–93, https://doi.org/10.1016/j.ultramic.2004.11.014.
[14] M.K. Miller, S.S. Babu, M.G. Burke, Intragranular precipitation in alloy 718, Mater. Sci. Eng. A 270 (1999) 14–18.
[15] C. Slama, C. Servant, G. Cizeron, Aging of the Inconel 718 alloy between 500 and 750 °C, Mater. Res. 12 (1997).
[16] J.M. Oblak, D.F. Paulonis, D.S. Duvall, Coherency strengthening in Ni base alloys hardened by DO_{22} precipitates, Metall. Trans. 5 (1974).
[17] D.P. Mcallister, Shearing Mechanisms and Complex Particle Growth in Nickel Superalloy 718, (2016).
[18] C. Slama, M. Abdellaoui, Structural characterization of the aged Inconel 718, J. Alloys Compd. 306 (2000) 277–284.
[19] D. Mukherji, R. Gilles, B. Barbier, D. Del Genovese, B. Hasse, Lattice misfit measurement in Inconel 706 containing coherent g′ and g″ precipitates, Scr. Mater. 48 (2003) 333–339.
[20] T.M. Smith, P. Bonacuse, J. Sosa, M. Kulis, L. Evans, A quantifiable and automated volume fraction characterization technique for secondary and tertiary γ′ precipitates in Ni-based superalloys, Mater. Charact. 140 (2018) 86–94, https://doi.org/10.1016/j.matchar.2018.03.051.
[21] W.H. Peter, P. Nandwana, M. Kirka, R.R. Dehoff, W. Sames, D. Erdman, Understanding the Role of Hot Isostatic Pressing Parameters on the Microstructural Evolution of Ti-6Al-4V and Inconel 718 Fabricated by Electron Beam Melting, ORNL/TM-2015/77, (2015).
[22] C. Notthoff, M. Winterer, A. Beckel, M. Geller, J. Heindl, Spatial high resolution energy dispersive X-ray spectroscopy on thin lamellas, Ultramicroscopy 129 (2013) 30–35, https://doi.org/10.1016/j.ultramic.2013.02.008.
[23] S.T. Wlodek, R.D. Field, The Effects of Long Time Exposure on Alloy 718, (1994).
[24] C. Ophus, J. Ciston, Correcting nonlinear drift distortion of scanning probe microscopy from image pairs with orthogonal scan directions, Ultramicroscopy (2015), https://doi.org/10.1016/j.ultramic.2015.12.002.
[25] Adaptive Threshold Plug-in - ImageJ, (n.d.). https://sites.google.com/site/qingzongtseng/adaptivethreshold.
[26] P.J. Phillips, D. Mcallister, Y. Gao, D. Lv, R.E.A. Williams, B. Peterson, Y. Wang, Nano g′/=g″ composite precipitates in Alloy 718, Appl. Phys. Lett. 100 (2012), https://doi.org/10.1063/1.4721456.
[27] J. Brocher, T. Wagner, BioVoxxel Toolbox, http://imagej.net/BioVoxxel_Toolbox, (2015).
[28] S. Zafari, T. Eerola, J. Sampo, H. Kalviainen, H. Haario, Segmentation of overlapping elliptical objects in silhouette images, IEEE Trans. Image Process. 24 (2015) 5942–5952.
[29] G. Loy, A. Zelinsky, Fast radial symmetry for detecting points of interest, IEEE Trans. Pattern Anal. Mach. Intell. 25 (2003) 959–973.
[30] C. Jung, C. Kim, Segmenting clustered nuclei using H-minima transform-based marker extraction and contour parameterization, IEEE Trans. Biomed. Eng. 576 (2010) 2600–2604.
[31] M. Pilu, A. Fitzgibbon, R. Fisher, Ellipse-specific direct least-square fitting, Proc. 3rd IEEE Int. Conf. Image Process, 1996, pp. 599–602.
[32] J. Russ, R. Dehoff, Practical Stereology, 2nd ed., Plenum Press, New York, 1986.
[33] G.E. Pellissier, S.M. Purdy, Stereology and quantitative metallography, ASTM Spec. Tech. Publ. 504 (1971) 3–36.
[34] H. Demers, N. Poirier-Demers, A. Couture, D. Joly, M. Guilmain, N. De Jonge, D. Drouin, Three-dimensional electron microscopy simulation with the CASINO Monte Carlo software, J. Scanning Microsc. 33 (2011) 135–146, https://doi.org/10.1002/sca.20262.
[35] D. Joy, Beam interactions, contrast and resolution in the SEM, J. Microsc. 136 (1984) 241–258.
[36] K.D. Vernon-Parry, Microscopy: an introduction, III-Vs Rev. 13 (2000) 40–44.
[37] J.E. Hilliard, J. Cahn, An evaluation of procedures in quantitative metallography for volume-fraction analysis, Trans. Metall. Soc. AIME 221 (1961).
[38] P.M. Kelly, Quantitative electron microscopy, Focal Point. (1982) 5.
[39] J.L. McCall, W.M. Mueller, Microstructural Analysis - Tools and Techniques, Plenum Press, New York, 1973.
[40] T.P. Gabb, J. Gayda, D.F. Johnson, R.A. Mackay, R.B. Rogers, C.K. Sudbrack, E. Kang, Comparison of γ-γ′ Phase Coarsening Responses of Three Powder Metal Disk Superalloys, (2017).